

The Faint Host Galaxies of CIV Absorbers at $z > 5$

Kristian Finlator^{1,2,7}, Caitlin Doughty¹, Zheng Cai³, Gonzalo Díaz^{4,5,6}

¹ *New Mexico State University, Las Cruces, NM, USA*

² *Cosmic Dawn Center (DAWN), Niels Bohr Institute, University of Copenhagen / DTU-Space, Technical University of Denmark*

³ *Department of Astronomy and Center for Astrophysics, Tsinghua University, Beijing, 100084, China*

⁴ *Gemini Observatory, Southern Operations Center, La Serena, Chile*

⁵ *Instituto de Ciencias Astronómicas, de la Tierra y del Espacio (ICATE), San Juan, Argentina*

⁶ *Consejo de Investigaciones Científicas y Técnicas (CONICET), San Juan, Argentina*

⁷ *finlator@nmsu.edu*

Accepted XXX. Received YYY; in original form ZZZ

ABSTRACT

We explore the expected galaxy environments of CIV absorbers at $z > 5$ using the *Technicolor Dawn* simulations. These simulations reproduce the observed history of reionization, the $z \sim 6$ galaxy stellar mass function, the Ly α forest transmission at $z > 5$, and the SiIV column density distribution (CDD) at $z \approx 5.5$. Nonetheless, the CIV CDD remains underproduced. Comparison with observed CII/SiII equivalent width ratios and the CII line incidence suggests that a low carbon yield accounts for some, but not all, of the CIV discrepancy. Alternatively, a density-bounded escape scenario could harden the metagalactic ionizing background more dramatically even than binary stellar evolution, boosting the CIV CDD into near-agreement with observations. In this case galaxies ionize more efficiently and fewer are required to host a given high-ionization absorber. Absorbers' environments therefore constrain ionizing escape. Regardless of the escape scenario, galaxies correlate with CIV absorbers out to 300 proper kpc (pkpc). The correlation strengthens independently with galaxy luminosity and CIV column density. Around strong systems ($\log(N_{\text{CIV}}/\text{cm}^{-2}) > 14$), the overdensity of galaxies with $M_{\text{UV}} < -18$ or $\log(L_{\text{Ly}\alpha}/\text{erg s}^{-1}) > 41.9$ declines from 200–300 within 100 pkpc to 40–60 within 250 pkpc. The previously-suggested association between strong CIV absorbers and Ly α emitters at $z > 5$ is not expected. It may arise if both populations inhabit large-scale voids, but for different reasons. Although most neighboring galaxies are too faint for *HST*, *JWST* will, with a single pointing, identify ~ 10 neighboring galaxies per strong CIV absorber at $z > 5$. Ground-based tests of these predictions are possible via deep surveys for Ly α emission using integral field units.

Key words: reionization — galaxies: formation — galaxies: evolution — galaxies: high-redshift — intergalactic medium — quasars: absorption lines

1 INTRODUCTION

Over the past twenty years, increasingly sophisticated surveys have uncovered thousands of galaxies that were in place and growing vigorously long before the Epoch of Cosmological Hydrogen Reionization (EOR) ended. The overall abundance and spatial distribution of young galaxies has been measured at luminosities less than 1% of L_* (Finkelstein et al. 2015; Bouwens et al. 2015; Santos et al. 2016; Drake et al. 2017; Livermore et al. 2017; Atek et al. 2018; Konno et al. 2018; Yue et al. 2018; Bhatawdekar et al. 2019; Khusanova et al. 2019; de La Vieuville et al. 2019), yielding critical constraints on star formation and feedback at early times. The emerging

consensus that faint galaxies were abundant during the EOR begs the question as to what feedback processes regulated their growth, and what, if anything, they contributed to cosmological hydrogen reionization.

Theoretical models indicate that the primary mechanism for regulating the growth of galaxies in dark matter halos with masses $M_h > 10^9 M_\odot$ is galactic outflows (Schaye et al. 2010; Somerville & Davé 2015). Outflows, in turn, leave signatures in the circumgalactic medium (CGM) that are sensitive probes of kinetic and radiative feedback. For example, hydrodynamic simulations have shown that metal absorbers are severely underproduced if outflows are absent (Oppenheimer & Davé 2008), that the

geometric cross section for neutral hydrogen absorption is enhanced by outflows (Faucher-Giguère et al. 2015), that the abundance of high-ionization absorbers is sensitive to outflow velocities (Keating et al. 2016), and that models in which more stars form tend to produce more metals and therefore stronger metal absorbers (Rahmati et al. 2016).

While these ensemble studies leverage well the growing catalog of high-ionization EOR absorbers that have been identified over the last decade, less progress has been made in understanding the relationship between individual EOR galaxies and their respective CGM. What sort of absorbers are found near galaxies of differing luminosities, and what sort of galaxies are expected near absorbers of differing strengths? How do answers to these questions constrain kinetic and radiative feedback?

Studies of galaxies' environments at $z=2-3$ have shown that bright ($\sim L_*$) galaxies possess enriched CGM whose metal column density falls smoothly with impact parameter (Steidel et al. 2010). By contrast, environmental studies at $z > 5$ suggest that strong CIV absorbers are found preferentially around faint galaxies rather than bright ones (Díaz et al. 2014). Does this apparent conflict reflect the difference between selecting galaxy-absorber pairs based on galaxy luminosity at low redshift versus CIV column density at high redshift, or does it indicate that the characteristic host galaxy of strong CIV absorbers evolves with time?

One suggested explanation is that faint galaxies dominated the metagalactic ionizing ultraviolet background (UVB) during the EOR (Díaz et al. 2014). As a CIV system's column density increases with both metallicity and UVB amplitude, faint galaxies could dominate the environments of strong CIV absorbers either by ejecting more metals than bright galaxies do, or by releasing more ionizing light into their environments. If this interpretation is correct, then it supports an outsized role for faint galaxies in driving reionization and UVB evolution. Indeed, encouraging qualitative support for the idea that absorbers trace LyC emission was recently presented by Meyer et al. (2019), who found evidence for local-scale Lyman- α forest opacity fluctuations in the vicinity of strong CIV absorbers.

The possibility of using the environments of high-ionization metal absorbers to trace ionizing flux from faint galaxies represents an intriguing complement to existing efforts. By far the most popular current approach involves measuring the galaxy luminosity function (LF), estimating the overall Lyman continuum (LyC) emissivity of all galaxies, and comparing it to the predicted recombination rate of the intergalactic medium (IGM). This method (for example, Madau et al. 1996) has been used to show that, subject to assumptions regarding the extrapolated abundance of faint galaxies, their intrinsic LyC emissivity ξ_{ion} (that is, the ratio of the ionizing to non-ionizing luminosity), the fraction f_{esc} of LyC light that escaped into the IGM, and the overall IGM recombination rate (Pawlik et al. 2009; Finlator et al. 2012; Jeason-Daniel et al. 2014), star formation in young galaxies had the potential to drive hydrogen reionization to completion (Yan & Windhorst 2004; Robertson et al. 2010, 2015; Haardt & Madau 2012; Bouwens et al. 2016; Finkelstein et al. 2019).

Whether the values of ξ_{ion} and f_{esc} that result from these analyses are realistic is more difficult to answer observationally (Ellis 2014). Evidence that young galaxies had the po-

tential to sculpt their environments comes from the strength of their emission lines, which reflect ionizing light from massive young stars that has been re-processed in the interstellar medium (ISM) (Bromm et al. 2001). The recent detection of strong line emission from galaxies at $z > 4$ (Stark et al. 2015; Bouwens et al. 2016; Smit et al. 2016; Rasappu et al. 2016) constrains the parameter combination $\xi_{\text{ion}}(1 - f_{\text{esc}})$ to be larger than expected for active, low-metallicity galaxies, but it does not directly trace the amount of ionizing flux escaping into the IGM.

Measurement of galaxies' non-ionizing ultraviolet continua, when modeled using stellar population synthesis techniques, can be used to constrain the product $\xi_{\text{ion}}f_{\text{esc}}$ (Duncan & Conselice 2015; Chisholm et al. 2019). Consistent with other studies, these efforts support the possibility that early galaxies packed sufficient firepower to complete reionization. However, results still depend on an extrapolation from the non-ionizing to the ionizing stellar continuum, which is in turn sensitive at the \sim factor-of-two level to uncertainties in the underlying stellar populations.

At $z < 4$, the relatively-transparent IGM allows direct detection of LyC flux (Inoue & Iwata 2008), yielding a more direct constraint on the product $\xi_{\text{ion}}f_{\text{esc}}$ (Rigby et al. 2019, and references therein). In a comprehensive analysis of ground-based spectroscopic measurements of bright galaxies at $z \sim 3$, Steidel et al. (2018) report a characteristic escape fraction of $f_{\text{esc}} = 9 \pm 1\%$. A central limitation in these results is that the galaxies at $z \leq 4$ for which leaking ionizing flux is directly detected may not be representative of the faint systems that dominated the UVB at $z \geq 5$, particularly if $f_{\text{esc}} < 5\%$ (Finkelstein et al. 2019).

The idea that bright galaxies, even if somewhat leaky, may not dominate the UVB is further underscored by Kakiichi et al. (2018), who detected a statistical association between transparent regions in the Ly α forest (LAF) and Lyman Break galaxies (LBGs) at $5.3 \lesssim z \lesssim 6.4$. They find that, while the LBGs themselves cannot provide the necessary flux to ionize the local LAF, faint galaxies that are presumably clustered about them may be able to provided that $f_{\text{esc}} \geq 8\%$. This pathbreaking study provides independent support for the view that, at $z > 5$, the LAF opacity reflects local-scale UVB fluctuations (see also Davies et al. 2018; Becker et al. 2018; Kashino et al. 2019). Nonetheless, its result is qualitatively similar to the overall one: an unseen population of galaxies with unknown LyC emissivity must be invoked in order to explain the observed properties of the high- z LAF.

The escape fraction f_{esc} from faint galaxies may be faithfully sampled via followup spectroscopy of long-duration gamma-ray bursts (GRBs), which are associated with core-collapse supernovae (Hjorth et al. 2003). Tanvir et al. (2019), applying a method developed by Chen et al. (2007), have shown that GRB spectra inevitably show evidence for proximate damped Ly α absorbers (DLAs), which are optically thick to LyC. They estimate a mean f_{esc} from the regions where GRBs originate of much less than 1%. If this number applies generally to star-forming regions in the EOR, then not only does it conflict with studies that directly detect an association between galaxies, absorbers, and the LAF (Kakiichi et al. 2018; Meyer et al. 2019), it rules out the galaxy-driven reionization hypothesis.

In this work, we explore how deep galaxy surveys near

strong CIV absorbers trace the release of metals and ionizing flux from faint galaxies. As a by-product, we will show that the next generation of deep followup surveys using Integral Units as well as the *James Webb Space Telescope* (*JWST*) will uncover faint galaxies $\sim 100\times$ more efficiently than blank-field surveys when they target the environments of strong metal absorbers. While the actual source densities in these areas will be biased, they will nonetheless probe the faint end of the overall LF indirectly through comparison with models that treat the absorber-galaxy relationship realistically.

In Section 2, we review our simulations. In Section 3, we highlight improvements with respect to our previous work through comparisons between predictions and observations of the galaxy stellar mass function, the history of reionization, the evolution of the intergalactic medium, and the abundance of metal absorbers. We discuss evidence that adjustments either to the assumed ratio of carbon and silicon yields or to the geometry of ionizing escape may be required. We analyze the predicted relationship between galaxies and absorbers in Section 4. Finally, we summarize in Section 5.

2 SIMULATION

Our simulation is an update to the *Technicolor Dawn* calculations described in Finlator et al. (2018). It assumes the same cosmology in which $(\Omega_M, \Omega_\Lambda, \Omega_b, H_0, X_H) = (0.3089, 0.6911, 0.0486, 67.74, 0.751)$. However, it incorporates several adjustments to dynamic range and subgrid physics that were motivated by discrepancies with observations as discussed there. Here, we outline those updates and discuss their effects.

2.1 Adjustments to the Feedback Model

Our newest calculation models a $15h^{-1}\text{Mpc}$ volume with 2×640^3 mass resolution elements, and the UVB is modeled using 80^3 spatial resolution elements (“voxels”). This “p115n640RT80NF24” simulation treats roughly twice the cosmological volume as our previous best calculation (Finlator et al. 2018) with the same mass and spatial resolution, enabling us to account more completely for rare, bright galaxies without compromising on our ability to capture faint galaxies and model the post-reionization LAF.

We scale down the rate at which star-forming galaxies eject gas and metals by 0.2 dex with respect to Finlator et al. (2018). This rate is governed by the mass-loading factor η , which is the ratio of the rate at which galaxies eject gas to their star formation rate. Previously, we adopted this parameter’s dependence on stellar mass $\eta(M_*)$ from the high-resolution simulations of Muratov et al. (2015) without adjustment. However, Muratov et al. (2015) note that the normalization of their published calibration carries an uncertainty of 0.2 dex, which roughly matches the discrepancy between our predictions and observations of the galaxy stellar mass and rest-frame UV LFs at $z \sim 6$ (cf. Figures 3 and 4 of Finlator et al. 2018). For our updated simulations, we therefore adopt

$$\eta(M_*) = 0.63 \times 3.6 \left(\frac{M_*}{10^{10} M_\odot} \right)^{-0.35}. \quad (1)$$

With this adjustment, the galaxies in our simulation produce slightly more stars and metals. They also produce more ionizing photons because we have not changed the underlying emissivity model, which is based on a modified version of YGGDRASIL (Zackrisson et al. 2011) as described in Finlator et al. (2018). In order that it predict roughly the same reionization history while also reproducing recent measurements of the mean transmission in the post-reionization LAF (Bosman et al. 2018), we adjust our escape fraction model to

$$f_{\text{esc}}(z) = 0.166 \left(\frac{1+z}{6} \right)^{2.65}, \quad (2)$$

and we cap $f_{\text{esc}}(z)$ at a maximum value $f_{\text{esc,max}} = 0.31$. This $f_{\text{esc}}(z)$ model is slightly lower than our previous high-resolution model at all redshifts, and it is consistent with recent observational inferences. For example, it predicts $f_{\text{esc}} = 0.057$ at $z = 3$, which lies below the observationally inferred value for bright galaxies at that redshift (0.09 ± 0.01 ; Steidel et al. 2018). Likewise, it predicts $f_{\text{esc}} = 0.13$ at $z = 4.5$, consistent with the upper limit of 0.13 inferred from observations of H α emission at $z = 4-5$ (Bouwens et al. 2016). While these agreements support the emerging view that galaxies could readily have driven reionization and dominated the post-reionization UVB (Robertson et al. 2010, 2015; Bouwens et al. 2016; Planck Collaboration et al. 2016; Finkelstein et al. 2019), Equation 1 remains an assumption that must be tested through more detailed observations. As a starting point, $f_{\text{esc}}(z)$ is assumed to be energy-independent; we will explore relaxing this assumption below.

3 COMPARISONS WITH PREVIOUS RESULTS

3.1 Observations of Galaxies

We now demonstrate that, with the adjustments described in Section 2.1, our new simulation yields improved agreement with observations of the galaxy stellar mass function, the history of reionization and the post-reionization LAF, and the abundance of metals in the high-redshift CGM. In order to make these comparisons, we apply the methods for identifying simulated galaxies and modeling absorption in the IGM/CGM previously described in Finlator et al. (2018), to which the reader is referred for details on post-processing. As in that work, galaxy luminosities M_{UV} refer to the rest-frame 1500Å luminosity and are computed as AB magnitudes.

We begin with the galaxy stellar mass function (SMF) at $z = 6$. In Figure 1, we compare predictions from two previously-published simulations and our newest one versus observations. Comparing our previous calibration (p112n512RT64NF24; magenta) versus our most recent one (p115n640RT80NF24; black) reveals that suppressing outflows by 0.2 dex (Equation 1) boosts the predicted stellar mass of all galaxies by a similar factor, yielding improved agreement with the deepest available measurements. As our new simulation subtends nearly twice the cosmological volume, it also extends to slightly higher masses, slightly improving overlap with the observed dynamic range.

In an earlier work (Finlator et al. 2016), we presented a smaller, “p7.5n340RT40” simulation that readily reproduced

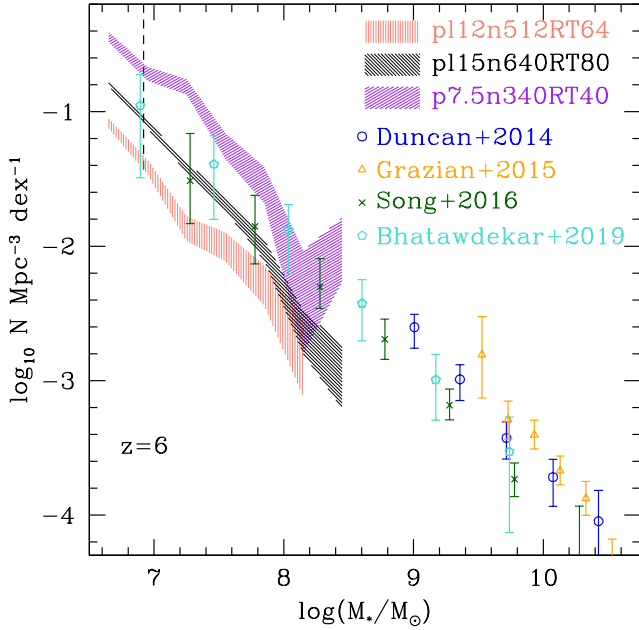


Figure 1. Stellar mass functions at $z = 6$ in our previous and updated simulations versus observations; the pl15n640RT80 simulation (black) represents our most up-to-date calibration. The vertical tickmark indicates the 64-star particle mass resolution limit for all simulations. Turquoise pentagons are from Bhatwadekar et al. (2019) and reflect their point-source incompleteness corrections; other points represent previous observations as indicated in the legend (Duncan et al. 2014; Grazian et al. 2015; Song et al. 2016).

the observed CIV abundance. By comparing with measurements of the $z \sim 6$ SMF that have been carried out since that work was published, we now see that, while it reproduced the observed CIV abundance at $z > 5$, it may have done so in part by overproducing stars and therefore metals (Rahmati et al. 2016).

The tendency for high-redshift star-forming galaxies to be strong line emitters opens up the possibility of quantifying the environments of high-redshift metal absorbers using narrow-line selection in addition to broadband selections (Cai et al. 2017b). As our simulations do not capture the detailed physics associated with emission and diffusion of Ly α , we model the outcome of these processes in post-processing via an empirical calibration.

For each simulated galaxy, we obtain the expectation value of its Ly α equivalent width ($EW_{Ly\alpha}$) from its stellar mass using Equation 22 of Oyarzún et al. (2017).¹ We show the resulting M_{UV} - $EW_{Ly\alpha}$ relationship in the inset panel of Fig. 2. The intrinsic scatter in $M_{UV}(M_*)$ generates scatter in $EW_{Ly\alpha}(M_{UV})$, but broadly the adopted values are in the range 40–80 Å. Observations are incomplete in the luminosity range spanned by the model. For example, Fig. 6 of Drake et al. 2017 indicates that their $z \approx (5, 5.5, 6.64)$ Ly α

¹ This step is largely an extrapolation because only a few of our simulated galaxies at $z = 5.75$ have $M_* > 10^8 M_\odot$, the range that dominates the Oyarzún et al. (2017) observations.

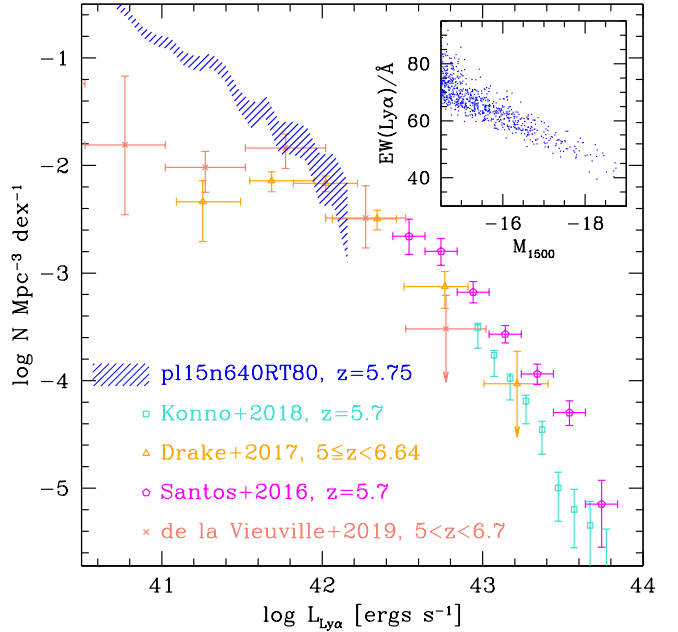


Figure 2. The shaded blue region shows the predicted Lyman- α luminosity function at $z = 5.75$ (see text); its width indicates \sqrt{N} uncertainty. Orange triangles, turquoise squares, magenta pentagons, and salmon crosses indicate observations by Drake et al. (2017), Konno et al. (2018), Santos et al. (2016), and de La Vieuville et al. (2019), respectively. All observations have been adjusted to our assumed cosmology. The predicted and observed LFs are in good agreement where observational incompleteness is not severe.

LFs are 50% complete at $(\log(L_{Ly\alpha}/\text{erg s}^{-1}) = (42.0, 42.3, 42.7)$. Nonetheless, the satisfactory agreement between the predicted and observed Lyman- α luminosity functions in Fig. 2 is encouraging. As no *ad hoc* calibration has been applied to this analysis, the tentative agreement can be viewed as a test of the simulated UV LF and $M_{UV} - M_*$ relations, which, when combined with the observed dependence of the Ly α equivalent width on stellar mass at $3 < z < 4.6$, are what yield the prediction in Fig. 2.

3.2 Observations of HI Reionization

The top panel of Figure 3 shows that the updated simulation (pl15n640RT80NF24; solid black) predicts roughly the same overall reionization history as the previous one (pl12n512RT64; dashed salmon). In detail, reionization occurs slightly later in the newer run, yielding improved agreement with constraints on the pre-overlap neutral fraction, but the difference is not large compared to uncertainties. By contrast, the bottom panel shows that the predicted mean transmission in the LAF $T_{Ly\alpha}$ during the interval $5 < z < 6$ is in much better agreement with observations (Bosman et al. 2018; Eilers et al. 2018). The disagreement between our previous simulation and observations of $T_{Ly\alpha}$ is unlikely to reflect primarily resolution limitations because detailed convergence studies indicate that, for our choice of mass resolution and simulation volume, $T_{Ly\alpha}$ should be converged to $\leq 10\%$ (D’Aloisio et al. 2018; Oñorbe et al. 2017). We con-

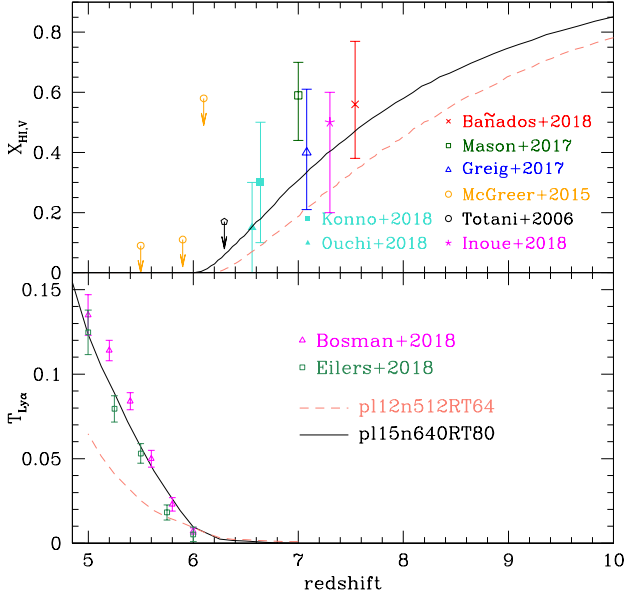


Figure 3. The history of reionization (top figure) and the mean transmission in the Lyman- α forest in our previous and new simulations. Both are in good agreement with the bulk of the measurements of the volume-averaged neutral hydrogen fraction prior to overlap (top panel), but our most recent calculation also yields a more realistic UVB in the post-overlap phase (bottom panel).

clude that our newest simulation yields a UVB whose pre-overlap growth rate and post-overlap amplitude are suitably realistic for studies of the EOR CGM.

3.3 Observations of Metal Absorbers

The improvements in Figures 1–3 allow us ask to what extent small, observationally-permitted adjustments to the overall star formation efficiency and ionizing escape fraction could bring the SiIV and CIV CDDs predicted in our previous work into improved agreement with observations. We address these questions directly in Figures 4–5.

Figure 4 confirms that, as expected, boosting the star formation efficiency and the UVB amplitude does increase the overall CIV production. Note that this comparison benefits from a realistic treatment for observational incompleteness. We assume, following results from simulations by D’Odorico et al. (2013), that the observed CIV census is (60, 70, 85, 100)% complete at $\log(N_{\text{CIV}}/\text{cm}^{-2}) = 13.3, 13.4, 13.5, 13.6$ and multiply the predicted abundance by this completeness function, interpolating to each column density. Extrapolating this trend so that completeness falls to zero at $\log(N_{\text{CIV}}/\text{cm}^{-2}) \leq 12.6$ causes the predicted turnover at low columns.

While our new simulation does produce overall more CIV than its predecessor, the predicted CDD still falls noticeably short of observations. Solving this problem by further boosting the UVB amplitude would compromise the excellent agreement with $T_{\text{Ly}\alpha}$ (Figure 3). Nor can the overall star formation efficiency be boosted, as this would overproduce the galaxy stellar mass function (Fig. 1).

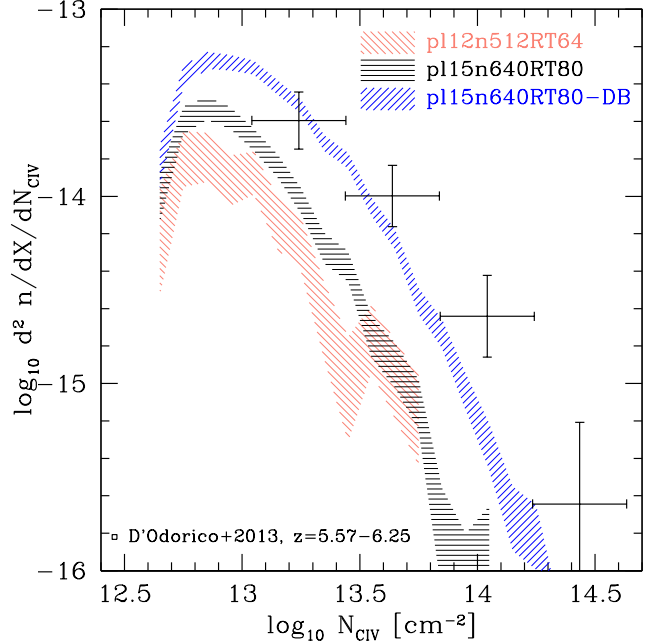


Figure 4. The predicted CIV column density distribution in three different scenarios versus observations. The black, p112n512RT64 region is an “out-of-the-box” representation of predictions from Finlator et al. (2018). The salmon, p115n640RT80 region is an “out-of-the-box” CDD compiled from our updated simulations. The blue, p115n640RT80-DB region shows that a density-bounded escape fraction model significantly boosts CIV. Observations are from D’Odorico et al. (2013).

Could the offset indicate problems with the assumed metal yields? In order to test whether an arbitrary adjustment to the overall metal yield² is indicated, we compare in Figure 5 the observed and simulated SiIV CDDs at a similar redshift. This comparison also accounts for observational incompleteness: we scale the column densities in the CIV incompleteness function using the matched optical depth method so that the SiIV completeness at any column density is the same as the CIV completeness at a column density that is a factor 2.432 higher. Taking this into account, we find that, whereas our previous simulation systematically underproduced SiIV, the updated prediction lies within 1σ of observations at all columns.

Figures 4–5 suggest that, if the assumed overall metal yield is correct, then our simulations cannot simultaneously match observations of the CIV and SiIV CDDs: boosting the UVB amplitude or the stellar mass density in order to match the CIV CDD would lead us to overproduce SiIV. This may, for example, contribute to the result discussed by Codoreanu et al. (2018), whose reference simulation reproduced the observed high-redshift CIV CDD but overproduced SiIV. We conclude that matching the observed SiIV and CIV CDDs simultaneously requires adjustments either to the *relative* carbon and silicon yields, or to the slope of the UVB.

² The overall metal yield is the ratio between the mass of new metals of all species ejected to the mass of long-lived stars formed (Tinsley 1980).

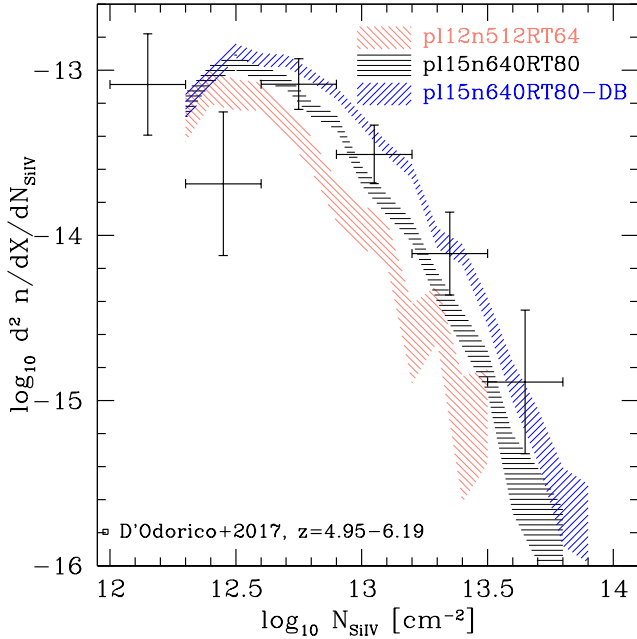


Figure 5. The predicted SiIV column density distribution in three different scenarios versus observations. The black, pl12n512RT64 region is an “out-of-the-box” representation of predictions from Finlator et al. (2018). The salmon, pl15n640RT80 region is an “out-of-the-box” CDD compiled from our updated simulations. The blue, pl15n640RT80-DB region shows that a density-bounded escape fraction model boosts SiIV production somewhat. Observations are from V. D’Odorico (private communication).

In order to explore the former possibility, we select co-spatial CII and SiII absorbers at $z = 6$ in simulations and between $5.75 < z < 6.25$ in the Becker et al. (2019) observations and compare the distribution of CII/SiII equivalent width (EW) ratios in Figure 6. As low-ionization absorbers tend to have weak ionization corrections (Becker et al. 2011), the EW ratio of co-spatial absorbers traces the underlying metal abundance ratio. The weighted mean observed EW ratio at $z \sim 6$ is 0.94 (dashed segment in both panels). Selecting simulated systems using a cutoff of 0.05 \AA in $\text{EW}(\text{CII}, \text{SiII})$, we find mean predicted ratios of (0.77, 0.54). Given that the measured abundance ratio of C/Si in the solar photosphere is 3.56 (Asplund et al. 2009), the model therefore agrees qualitatively with observations that the high-redshift C/Si abundance ratios are subsolar (see also Becker et al. 2011, Table 6). Quantitatively, however, they are rather too subsolar; the predicted yield ratio of C to Si could be increased by 22–75%.

Boosting the assumed carbon yields would increase the abundances of both CII and CIV. As the tendency for low- and high-ionization ions to evolve differently at $z > 5$ (Becker et al. 2011; Cooper et al. 2019) may encode key insight into early IGM enrichment and reionization, we compare in Fig. 7 the predicted and observed line incidences dN/dX of CII and CIV. For CII, we adopt the catalog of low-ionization absorbers spanning $z = 5.75\text{--}6.25$ by Becker et al. (2019) and select systems with $\text{EW}_{\text{CII}} > 0.08 \text{ \AA}$. This catalog probes an absorption path length of $\Delta X = 65.34$ in our

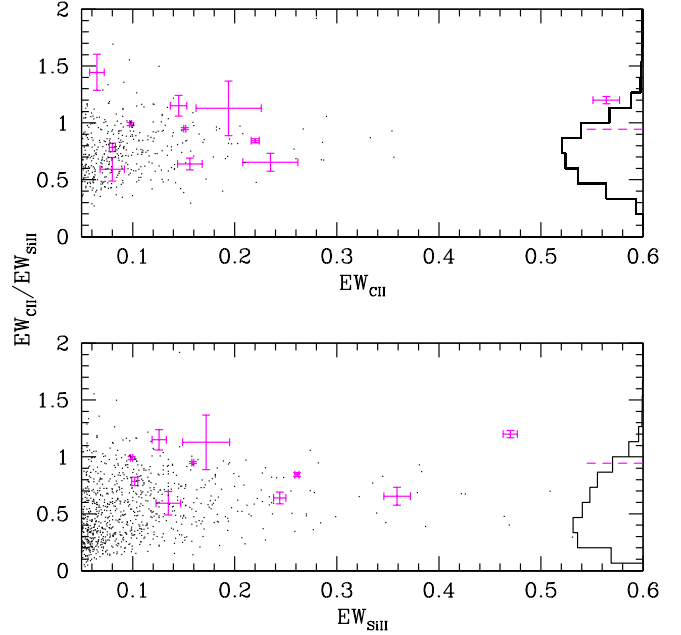


Figure 6. The distribution of CII/SiII equivalent widths versus CII (top) and SiII (bottom) equivalent width in the simulation at $z = 6$ (dots) versus observations spanning $5.75 < z < 6.25$ (Becker et al. 2019). Histograms collapse the predicted distribution along the x-axis after applying a minimum equivalent width of 0.05 \AA . The dashed segment indicates the weighted mean observed ratio. Both panels indicate that the simulated CII/SiII ratios are biased low.

cosmology. For CIV, we obtain the observed line incidence of systems with column densities $13.5 < \log(N_{\text{CIV}}) < 14.5$ from the fit to Fig. 19 of D’Odorico et al. (2013). Adjusted to our cosmology, this yields $dN/dX(\text{CIV}) = 0.464 \pm 0.091$ for $5.3 < z < 6.2$. The simulated CIV and CII line incidences are compiled using the same cuts in equivalent width and column density. Incompleteness is modeled in CIV as before, while incompleteness in CII is modeled using a fit to Fig. 2 from Becker et al. (2019). Uncertainties are \sqrt{N} except in the case of the observed CIV line incidence, where we assume it is dominated by the uncertainty in the slope of the observed CIV column density distribution.

Without adjustments in post-processing, the magenta point labeled “ionization-bounded” in Fig. 7 indicates clearly that the simulation underproduces both CII and CIV. This supports the view that the assumed metal yield from supernovae and/or evolved stars is too low. Scaling all simulated C mass fractions up by a factor of $1.75\times$ (green arrow) brings the CII line incidence into agreement with observations while alleviating roughly half (in logarithmic units) of the CIV discrepancy.

3.4 A Model for Density-Bounded Escape

In this section, we ask whether physically-motivated changes to the way in which ionizing light escapes from galaxies could steepen the predicted UVB enough to yield simultaneous agreement with SiIV and CIV observations. While it is conventional to model the UVB under the as-

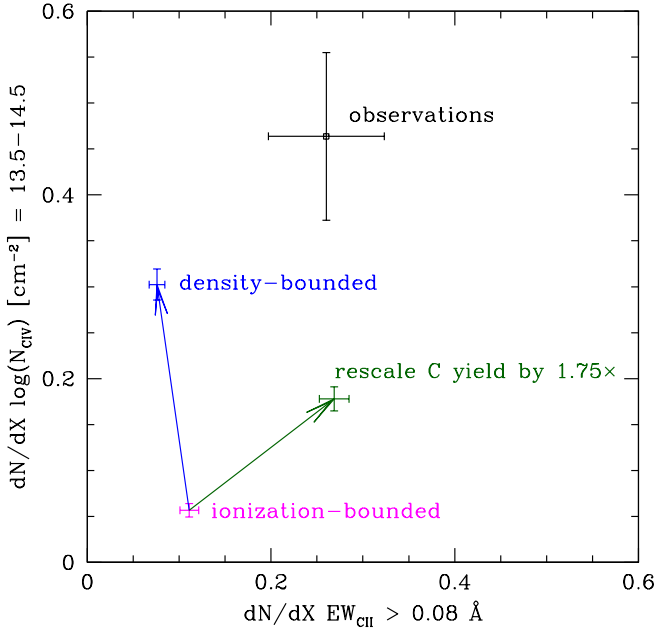


Figure 7. A comparison with joint constraints on the line incidences of CII and CIV. Observations of CII and CIV are from Becker et al. (2019) and D’Odorico et al. (2013), respectively. Without adjustment in post-processing, the simulation underproduces both ions. Rescaling simulated C abundances globally boosts CII into agreement with observations. A density-bounded escape model improves agreement with CIV while exacerbating the CII underproduction.

sumption that the escape of ionizing photons from galaxies is an energy-independent scalar f_{esc} (Bromm et al. 2001; Haardt & Madau 2012; Khaire & Srianand 2019), this model is not required *a priori*. Physically, the assumption of a scalar f_{esc} corresponds to a scenario in which ionizing flux escapes through transparent “holes” in the interstellar medium (ISM) which are in turn separated by opaque “walls” (Wise & Cen 2009). Equivalently, it may be imagined that a small fraction of massive stars lie “outside” the ISM (Conroy & Kratter 2012), although it has been argued that this particular effect may not dominate ionizing escape (Kimm & Cen 2014). Following Zackrisson et al. (2013), we refer to this scenario as the “ionization-bounded” escape model (IB). Direct evidence that some LyC flux escapes through optically-thin channels is provided by LyC-leaking galaxies for which Ly α emission is observed at the systemic velocity (Rivera-Thorsen et al. 2017; Izotov et al. 2018b; Vanzella et al. 2019). This signature is predicted in such scenarios theoretically (Behrens et al. 2014).

In order to explore the possible consequences of this widespread assumption, we consider the opposite extreme. In this “density-bounded” (DB) scenario, each star is separated from the ISM’s boundary by a thin layer of gas whose column density is tuned so that the overall escape of HI-ionizing flux matches the IB model, but the optical depth to more energetic photons

is lower.³ Evidence that ionizing flux may escape from high-redshift galaxies via density-bounded media comes from observations that high [OIII]/[OII] emission line flux ratios and weak [SII] emission are reliable predictors of LyC emission (Alexandroff et al. 2015; Izotov et al. 2016, 2018a; Fletcher et al. 2019; Vanzella et al. 2019). Additionally, Steidel et al. (2018) report that a representative sample of LyC-leaking galaxies at $z \sim 3$ do not show appreciable Lyman- α emission at the systemic velocity. We impose the DB scenario in post-processing as an adjustment to the UVB that is predicted on-the-fly. First, we compute the volume-averaged HI ionization rate $\langle \Gamma_{\text{HI}} \rangle$:

$$\langle \Gamma_{\text{HI}} \rangle \equiv \left\langle \int \frac{4\pi J_\nu}{h\nu} \sigma_\nu d\nu \right\rangle \quad (3)$$

where $\langle \rangle$ indicate a volume-average and the other quantities have their usual meanings. Figure 3 insures that this ionization rate, which turns out to be $3.37 \times 10^{-13} \text{s}^{-1}$ at $z = 5.75$, is realistic.

Next, we rescale the simulated galaxy UVB by the reciprocal of the assumed $f_{\text{esc}}(z = 5.75) = 0.227$ (i.e., $J_\nu \rightarrow J_\nu / f_{\text{esc}}$) and compute the HI column density that would return the same $\langle \Gamma_{\text{HI}} \rangle$. This is accomplished by solving the equations

$$\begin{aligned} \langle \Gamma_{\text{HI}} \rangle &\equiv \left\langle \int \frac{4\pi J_\nu}{f_{\text{esc}}(z = 5.75)h\nu} \exp(-\tau_\nu) \sigma_\nu d\nu \right\rangle \quad (4) \\ \tau_\nu &= \sigma_{\nu, \text{HI}} N_{\text{HI}} + \sigma_{\nu, \text{HeI}} N_{\text{HeI}} \quad (5) \end{aligned}$$

for N_{HI} . The obscuring gas column is assumed to be completely neutral with the same helium mass fraction as the simulation. The resulting HI column density turns out to be $4.91789 \times 10^{17} \text{cm}^{-2}$. This low column density would manifest observationally in the Lyman- α emission profile as a small velocity offset and narrow peak separation (Verhamme et al. 2015; Kakiichi & Gronke 2019; Kimm et al. 2019). We then re-scale our simulated UVB by the ratio $J_\nu \rightarrow J_\nu \exp(-\tau_\nu) / f_{\text{esc}}(\nu)$ at all frequencies and positions. This adjustment is approximate because it assumes that J_ν varies linearly with $\exp(-\tau_\nu)$. In reality, increasing the emissivity decreases the opacity by ionizing more gas, which in turn amplifies the overall boost to J_ν (McQuinn et al. 2011). The detailed, superlinear dependence of J_ν on the emissivity model can only be established via numerical simulations. Our heuristic model for DB escape is therefore conservative in the sense that small changes to $f_{\text{esc}}(z, \nu)$ at high energies will have a larger impact than we estimate on J_ν .

We confirm in the top panel of Figure 8 that the volume-averaged galaxy UVB in the IB scenario has an overall steeper spectral slope than in the DB scenario. The difference is strongest for energies < 4 Ryd, where f_{esc} varies most strongly with energy in the DB scenario. The top panel also indicates the ionization potentials for the ions that we consider. The impact on the LAF of switching between the two scenarios will be small by design, although a harder UVB will inevitably yield a qualitatively hotter IGM, which may eventually be detectable in the LAF (Boera et al. 2019). The impact on ions such as SiIV and CIV, which are more sensitive to high-energy photons, will clearly be much more significant.

³ Illustrations of these two escape scenarios are found in Figure 1 of Zackrisson et al. (2013) and Duncan & Conselice (2015).

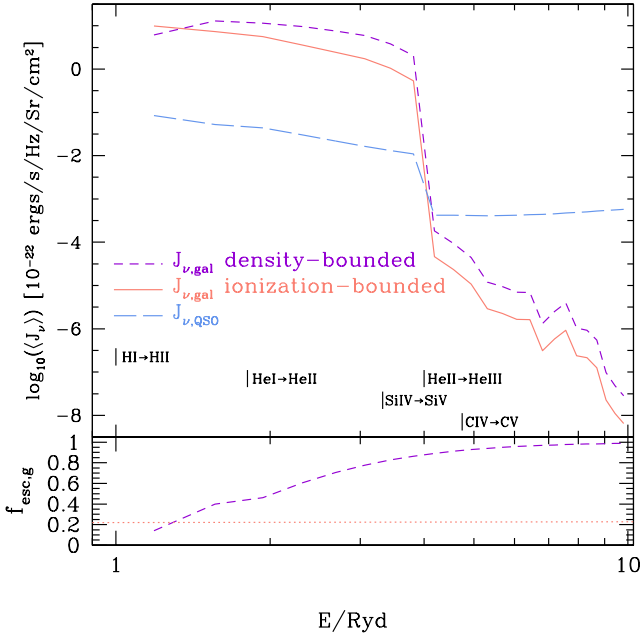


Figure 8. *Top:* The volume-averaged galaxy and quasar UVBs. In an “ionization-bounded” escape scenario (solid salmon), the galaxy UVB has an overall redder spectral slope than in a “density-bounded” scenario (dashed purple) even though the two yield precisely the same overall H I ionization rate. *Bottom:* In the ionization-bounded model, $f_{\text{esc}} = 0.22681$. By contrast, f_{esc} increases with energy in the density-bounded scenario even though its emissivity-weighted mean is unchanged.

In the bottom panel of Figure 8, we illustrate how the different spectral slopes in the top curve result from a different dependence of f_{esc} on energy. In the IB scenario, f_{esc} is a constant, whereas in the DB scenario it increases with energy, exceeding 50% at 2 Ryd and rising above 90% for He II-ionizing energies (> 4 Ryd). In essence, the DB model swaps low-energy flux for high-energy flux in order to achieve the same $\langle \Gamma_{\text{HI}} \rangle$.

We next ask whether the DB scenario can reconcile simulations with observations of the statistics of CIV and Si IV absorbers. To do this, we re-extract simulated quasar sightlines that are identical to the ones considered previously except that, at all positions, the metal abundance ratios are recomputed in the DB scenario. The quasar contribution to the UVB is retained without modification. We then identify and characterize synthetic metal absorbers in the same way as for the IB scenario.

The blue shaded region in Figure 4 shows that, by increasing the CIV fraction, the DB model roughly doubles each CIV absorber’s column density, nearly eliminating the CIV discrepancy. Similarly, we show in Fig. 4 that the DB model boosts the overall CIV line incidence into near-agreement with observations. This improvement comes at the expense of the C II, whose line incidence is pushed further away from the observed range.⁴ The DB model’s im-

⁴ As the impact on Si II is similar, the predicted distribution of C II/Si II equivalent with ratios (Figure 6) is only weakly sensitive to the choice of escape fraction model.

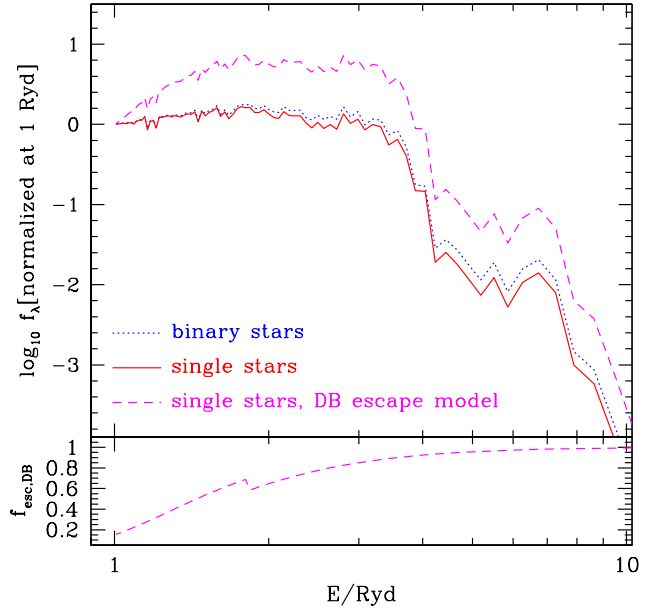


Figure 9. *Top:* The emissivity from a stellar population that has been forming stars at a constant rate for 100 Myr. The possibility of density-bounded escape is much more important at high energies than binary stellar evolution. *Bottom:* The escape fraction in the DB model.

pact on Si IV is weaker (Fig. 5) because Si IV probes softer photons than CIV.

The comparisons in Figures 4–5 reiterate that cosmological simulations confront grave difficulty in attempting to match simultaneously observations of the UVB, the galaxy stellar mass function, and the CIV and Si IV CDDs at high redshift. Although the CIV/Si IV abundance ratio is a tracer of the UVB’s spectral hardness that could constrain the relative contributions of galaxies and AGN (Finlator et al. 2016; Doughty et al. 2018), these figures suggest that it could alternatively probe the details of how ionizing light escapes from galaxies. In reality, as pointed out by Zackrisson et al. (2013), the IB and DB scenarios are opposite extremes and young stars will be separated from the CGM by sightlines spanning a distribution of column densities. Hence the question of how much CIV is generated by light from galaxies versus quasars depends on the nature of this unknown column density distribution.

This uncertainty is much more important for understanding high-ionization CGM ions than the effects of binary stellar evolution, which have been shown to increase the ionizing output of low-metallicity stellar populations and promote galaxy-driven reionization (Stanway et al. 2016; Ma et al. 2016; Rosdahl et al. 2018). The reason is that spectral filtering associated with DB escape steepens the emerging ionizing continuum more than binary stellar evolution steepens the intrinsic one. To illustrate this point, we compare in Figure 9 three hypothetical emerging spectra computed from version 2.2.1 of the Binary Population and Spectral Synthesis libraries (Eldridge et al. 2017). The red solid and blue dotted curves show spectra emerging from model galaxies that have been forming stars with $Z = 0.002$ at a

constant rate for $100M_{\odot} \text{ yr}^{-1}$; the default initial mass function “imf135_300” is used in both cases. When normalized to 1 Ryd, the tendency for binary stars to produce more ionizing flux at high energies is reproduced. However, comparison with the dashed magenta curve shows that the effect is dwarfed by that of a purely DB escape scenario: if we position the single-star model behind a neutral screen with a hydrogen column density of $3 \times 10^{17} \text{ cm}^{-2}$ and account for bound-free absorptions by both HI and HeI, then the escaping continuum steepens much more dramatically. In the bottom panel, we show the corresponding $f_{\text{esc}}(\nu)$, which rises from $f_{\text{esc}} = 15\%$ at the Lyman limit to 100% at 10 Ryd.

The uncertainty in the UVB joins other well-known uncertainties related to the stellar population and to the possible role of dust. Decreasing the metallicity of stellar populations generically amplifies and hardens their Lyman continua (Schaerer 2002). Meanwhile, the predicted C/Si supernova yield ratio $y_{\text{C}}/y_{\text{Si}}$ in the Nomoto et al. (2006) models varies nonmonotonically with metallicity, with an overall minimum of 0.68 and a maximum of 1.59 (Finlator et al. 2018, Table 3). The yield ratios are also sensitive at the $< 15\%$ level to our assumption of a 50% hypernova fraction (*ibid.*). We have not explored the implications of varying the initial mass function (IMF), although it has been shown previously that a more top-heavy IMF can boost both C and Si yields (Kulkarni et al. 2013). Finally, dust extinction generically reddens the emerging UV continuum, potentially counteracting the spectral hardening in the DB scenario.

These considerations highlight two unexplored avenues for future research. First, as noted by Berg et al. (2019), it is worth revisiting high-resolution simulations of high-redshift galaxies in order to quantify how f_{esc} varies with energy when both dust and a realistic distribution of ISM column densities are taken into account. Second, it is worth exploring how the predicted J_{ν} changes in synthesis models of the UVB (Faucher-Giguère et al. 2009; Haardt & Madau 2012; Khaire & Srianand 2019) if the conventional assumption of an IB escape scenario is relaxed.

4 THE ABSORBER-GALAXY CONNECTION

4.1 Detecting Hosts in the Far-UV Continuum

Having established that our simulation produces the correct number of galaxies and a UVB whose amplitude at the Lyman limit is realistic, we now turn to our motivating question of how bright the neighboring galaxies of high-redshift CIV absorbers are. We will show that the relationship depends on absorber strength, galaxy luminosity, distance, and the dependence of f_{esc} on energy. To enable this discussion, we identify simulated galaxies and compute their 1500\AA continuum luminosities (M_{UV}) as described in Finlator et al. (2018, §3.1) and then match them in position space with the simulated absorbers. Next, we compute the galaxy-absorber cross-correlation function $\xi_{\text{g-abs}}(r)$ for different combinations of minimum absorber strength and M_{UV} . The cross-correlation $\xi_{\text{g-abs}}(r)$ is computed as:

$$\xi_{\text{g-abs}}(r) \equiv \frac{1}{n_0} \frac{\Delta N(r)}{\Delta V} - 1, \quad (6)$$

where $\Delta N(r)$ is the mean number of galaxies within a finite spherical shell of volume ΔV located a distance r from an

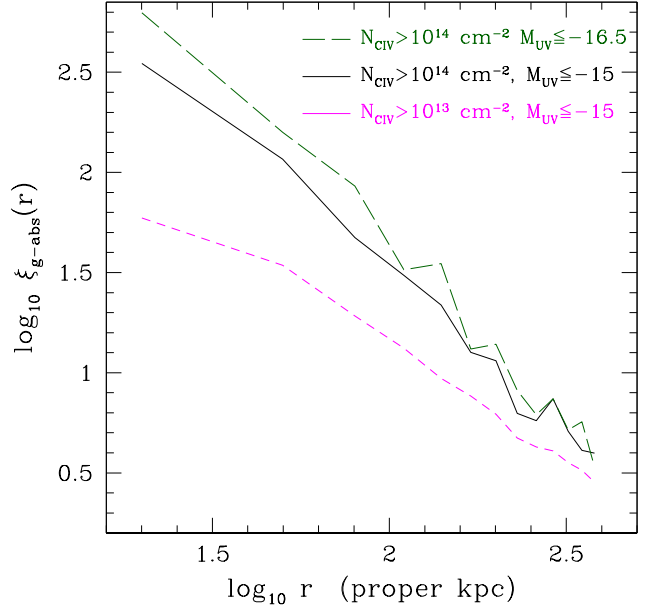


Figure 10. The CIV absorber-galaxy cross-correlation function at $z = 5.75$ in the DB escape scenario. Line styles and colors correspond to different combinations of minimum column density and luminosity as indicated. Galaxies and absorbers exhibit positive cross-correlation out to > 300 physical kpc, and the amplitude of the correlation function increases independently with absorber strength and galaxy luminosity.

absorber, and n_0 is the mean number density of galaxies averaged over the entire simulation volume. When computing $\xi_{\text{g-abs}}(r)$, we extract absorbers in the DB scenario because it reproduces the observed CIV CDD best; alternative adjustments to the model that boost CIV would yield very similar results. We will use “abundance” and “environment” interchangeably to refer to the local volume density of galaxies.

Figure 10 verifies that absorbers are positively correlated with galaxies out to distances of at least 300 proper kpc (pkpc). Moreover, the amplitude of $\xi_{\text{g-abs}}(r)$ increases with both luminosity and absorber strength. In other words, stronger absorbers have more galaxies in their neighborhoods, and bright galaxies cluster more strongly about absorbers than faint ones do.

This first hint that, even at early times, CIV absorbers form more efficiently around brighter galaxies seems qualitatively inconsistent with observational results that the host galaxies of strong, high-redshift absorbers tend to be faint (Díaz et al. 2011, 2014; Díaz et al. 2015; Cai et al. 2017b). However, these results are not necessarily in tension: if the dependence of clustering strength on luminosity is weak whereas the slope of the luminosity function’s faint-end is steep, one still expects to find more faint galaxies than bright ones about strong absorbers.

Note that, in order to map from the absorber’s position in velocity space to configuration space, we neglect its proper motion. For a typical velocity width of $\sim 50 \text{ km s}^{-1}$, this simplification could blur the predicted galaxy-absorber relation on scales of up to $\sim 75 \text{ pkpc}$. If this effect were severe, it would cause $\xi_{\text{g-abs}}(r)$ to flatten at small r . The absence of

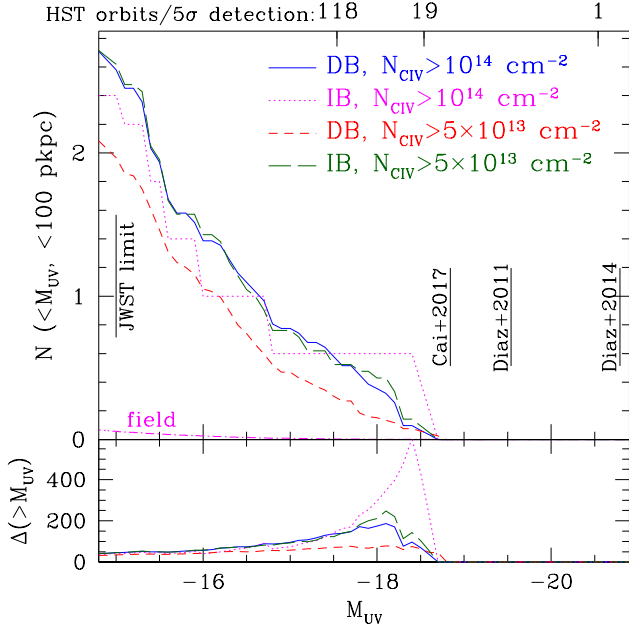


Figure 11. *Top:* The predicted average number of detectable galaxies within 100 pkpc of a CIV absorber at $z = 5.75$ as a function of M_{UV} . Curves corresponding to different combinations of minimum N_{CIV} and escape fraction scenario are identified in the legend. Irrespective of the column density or the choice of escape scenario, the probability of detecting a single galaxy does not approach unity for surveys that probe only to $M_{UV} \sim -17$, which is roughly *HST*’s blank-field limit. Vertical lines with references indicate the depths of published surveys. *Bottom:* The local galaxy overdensity $\Delta \equiv N_{CIV}/N_{\text{field}}$ as a function of luminosity.

such a feature in Fig. 10 indicates that this blurring is not a serious issue.

In order to explore how absorber environment may be quantified observationally, we group simulated galaxies that lie near absorbers (in three-dimensional space) into two bins of minimum CIV column density. Within each bin, we compute the mean cumulative number of galaxies that are located within 100 pkpc per absorber as a function of their minimum luminosity. For any given minimum luminosity, this number is an integral over the cross-correlation function $\xi_{g-\text{abs}}(r)$:

$$N(\leq M_{UV}, < 100\text{kpc}) = \int_0^{100\text{kpc}} 4\pi r^2 n_0 (1 + \xi_{g-\text{abs}}(r)) dr \quad (7)$$

The solid blue curve in Fig. 11 shows the cumulative luminosity function of neighbors for absorbers with $N_{CIV} > 10^{14} \text{ cm}^{-2}$. As in Fig. 10, the local galaxy abundance increases with absorber strength. Importantly, comparing the red short-dashed and green long-dashed curves reveals that local galaxy abundance also depends on the escape fraction model: if the escape fraction in the relevant energy regime is lower (as in the IB model), then more galaxies are expected per CIV absorber. This means measurements of absorbers’ environments constrain the high-energy emissivity of faint galaxies.

In order to quantify how absorbers’ environments vary with luminosity, we use the dot-dashed magenta curve in the top panel to show the “field” LF. This clearly indicates

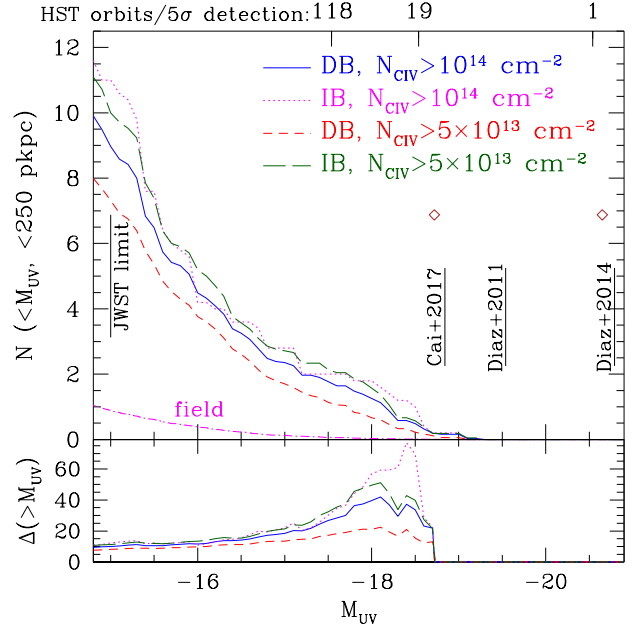


Figure 12. Same as Fig. 11, but for a maximum radius of 250 pkpc. More neighboring galaxies are predicted (top panel), but the mean galaxy overdensity out to this larger distance is lower (bottom panel). Diamonds indicate the luminosities of candidate host galaxies that have been identified within 250 pkpc of a strong CIV absorber at $z > 4.5$ (Díaz et al. 2014; Díaz et al. 2015; Cai et al. 2017b); their position on the vertical axis is arbitrary.

that galaxy abundance is much lower in a randomly-selected region than in the vicinity of strong CIV absorbers. By taking the ratio Δ of the absorber and field LFs, we recover the result from Fig. 10 that galaxy overdensity increases with luminosity. In particular, we show in the bottom panel of Fig. 11 that, within 100 pkpc, Δ rises from ≈ 50 for $M_{UV} = -15$ to ≈ 200 for $M_{UV} = -18$. Future simulations incorporating a larger cosmological volume will be necessary to determine whether the predicted local overdensity continues to rise to brighter luminosities.

Even though overdensity increases with luminosity, most of the absorbers’ neighbors are difficult to detect. The top axis of Fig. 11 converts the 1500Å luminosity to the number of *HST* orbits required to detect a point source at 5σ significance at $z = 5.75$. We computed this conversion using the online Exposure Time Calculator⁵ for the Advanced Camera for Surveys F805LP (z_{850}) filter assuming that the source radiates as a 25 Myr Simple Stellar Population with 0.4 times solar metallicity. Down to the *HST* blank-field limit ($M_{UV} \sim -17$), fewer than one associated galaxy per strong absorber is expected within a 100 pkpc radius despite the strong association between galaxies and absorbers. This radius corresponds to $17''$ at $z = 5.75$ in our cosmology, hence it is comparable to the field of view of the Keck Cosmic Web Imager (KCWI) and smaller than the or *HST*/ACS field of view when imaging through its ramp narrowband fil-

⁵ <http://etc.stsci.edu/etc/input/acs/imaging/>

ters. These instruments will not generally detect neighboring galaxies with a single pointing.

By contrast, we show in Figure 12 that a wider search radius—in this case, 250 pkpc—readily turns up more neighbors. The expected neighbor count does not vary linearly with the search area because galaxies are less clustered about absorbers at larger distances. This result was previously seen in Figure 10, and it can be recovered by comparing the bottom panels of Figures 11–12: the mean overdensity for galaxies with $M_{\text{UV}} = -18$ falls from ≈ 200 within 100 pkpc to ≈ 40 within 250 pkpc (see also Fig. 10). A single deep *HST*/ACS pointing (100–150 orbits in z_{850}) encloses this entire area and is predicted to uncover 2 galaxies. Redshift confirmation would require equally deep imaging in additional filters, so this approach remains impractical. Fortunately, *JWST* will soon prove extremely efficient at characterizing absorber environments: assuming a blank-field detection limit of $M_{\text{UV}} = -15$, *JWST*/NIRSPEC will, with a single deep pointing, identify ~ 10 neighboring galaxies per strong high-redshift CIV absorber.

Meyer et al. (2019) recently used an abundance-matching technique to estimate the typical M_{UV} and M_h of CIV hosts at $5.3 < z < 6.2$. Assuming a one-to-one relation between CIV absorbers and dark matter halos and a metal enrichment radius of 100 pkpc, they find that systems with $\log(N_{\text{CIV}}) > 13$ are associated with $> 10^{10} M_{\odot}$ halos and $M_{\text{UV}} < -16$ galaxies. We may compare this estimate directly with our model: In the DB model, the minimum luminosity such that at least one galaxy is contained within 100 pkpc of such an absorber at $z = 5.75$ is $M_{\text{UV}} < -14.5$, 1.5 magnitudes fainter than the Meyer et al. (2019) estimate. Although the two models differ in many ways, we suspect that the primary difference is the halo-absorber relationship: in our model, CIV clouds from individual galaxies overlap in such a way that, although absorbers and galaxies are physically associated out to scales of ≈ 300 pkpc (Fig. 10), the geometric cross-section per $M_h > 10^{10} M_{\odot}$ halo is smaller. Equivalently, our model predicts an abundant population of even fainter neighboring galaxies.

4.2 Comparison with Observations

To date, the published literature contains only a few robust associated galaxy-CIV absorber pairs at $z > 5$. Here we summarize their properties; where necessary we have converted to our simulation’s cosmology. Target 1 in Díaz et al. (2011) confirms a galaxy with $M_{\text{UV}} = -20.66 \pm 0.05$, $L_{\text{Ly}\alpha} = 8.01 \pm 0.55 \times 10^{42} \text{erg s}^{-1}$ lying at a transverse separation of 311.4 pkpc from the weak CIV absorber identified as System 10 in Table A3 of D’Odorico et al. (2013). Díaz et al. (2014) search around two strong absorbers and identify a candidate neighboring galaxy as a Ly α emitter (LAE) 103027+052419, which has a transverse separation from the CIV absorber of 212.3 pkpc (see also Díaz et al. 2015). Its UV continuum luminosity is $M_{\text{UV}} = -20.65 \pm 0.52$. Finally, Cai et al. (2017b) identified three LAE candidates around four strong CIV absorbers. Two of these were not detected in more recent measurements using an integral field unit (IFU) spectrograph (Díaz et al. 2020, *in press.*), but the candidate near the absorber at $z_{\text{CIV}} = 4.866$ has not yet been followed up using other instrumentation, so for the present we assume it to

be genuine. Its transverse separation from the absorber is 210 pkpc, and its continuum and Ly α line luminosities are $M_{\text{UV}} = -18.72 \pm 0.19$, and $L_{\text{Ly}\alpha} = 2.60 \pm 0.53 \times 10^{42} \text{erg s}^{-1}$. In total, these efforts have surveyed the environments near six strong CIV absorbers and identified three confirmed or candidate neighboring galaxies. Two of these lie within a transverse impact parameter of 250 pkpc of a strong absorber; their luminosities are indicated using diamonds in Figures 12 and 14.

Are these two neighbors expected? We cannot compare these statistics directly to our predictions owing to the fact that our simulation volume is not large enough to form galaxies brighter than $M_{\text{UV}} = -19$ at $z > 5$. However, given that Δ varies slowly with luminosity, we may simply assume a fiducial $\Delta = 40$ (bottom panel of Figure 12). Integrating the LF of Finkelstein et al. (2015, Table 4), we find that the mean comoving space density at $z = 5.75$ of galaxies brighter than $M_{\text{UV}} = (-19, -20)$ is $(9.25, 2.93) \times 10^{-4} \text{Mpc}^{-3}$. We would therefore expect an average of 0.74 ($\Delta/40$) neighboring galaxies brighter than $M_{\text{UV}} = -19$ within 250 pkpc of each strong absorber, or 4.44 galaxies about the six absorbers for which positive detections in follow-up surveys have been published to date. This order-of-magnitude level of agreement begs for improved constraints, which will be provided in the long term by observations using *JWST* and in the short term by surveys with IFUs.

4.3 Detecting Hosts in Lyman- α

In Fig. 13, we show that, irrespective of the choice of UVB or minimum CIV column density, the neighboring galaxies of strong CIV absorbers are expected to be predominantly faint LAEs. The predicted number of neighboring LAEs is sensitive to the absorber column and UVB model in the same ways that emerge from Fig. 11. Comparing the solid blue and short-dashed red curves reveals that the neighboring galaxies of stronger absorbers are brighter. Likewise, for a fixed column density, the density-bounded UVB predicts overall fainter galaxies because those absorbers are in this case associated with less rare systems.

As in the case of stellar continuum detections, we find in the bottom panel of Fig. 13 that the ratio Δ of the predicted number density of LAEs that lie within 100 pkpc of an absorber to the field LF is in the range of 100–500. In the case of the DB model and strong absorbers, Δ increases from ≈ 50 at the faintest luminosities currently probed ($L_{\text{Ly}\alpha} = 10^{41} \text{erg s}^{-1}$) to ≈ 200 at the brightest luminosities captured by our simulation. Whether Δ continues to grow at higher luminosities can only be established by simulations subtending larger cosmological volumes. It decreases with absorber strength and is overall higher in the IB model. Finally, we confirm in Figure 14 that a wider search area readily turns up more neighboring galaxies. In particular, a single deep VLT/MUSE pointing that probes to $10^{41.5} \text{erg s}^{-1}$ should uncover roughly three neighboring LAEs per strong CIV absorber at $z = 5.75$.

4.4 Discussion: The Possible CIV-LAE Association

Do strong CIV absorbers prefer the company of faint galaxies or bright ones? While only a few candidate neighboring galaxies are currently identified in the stellar continuum

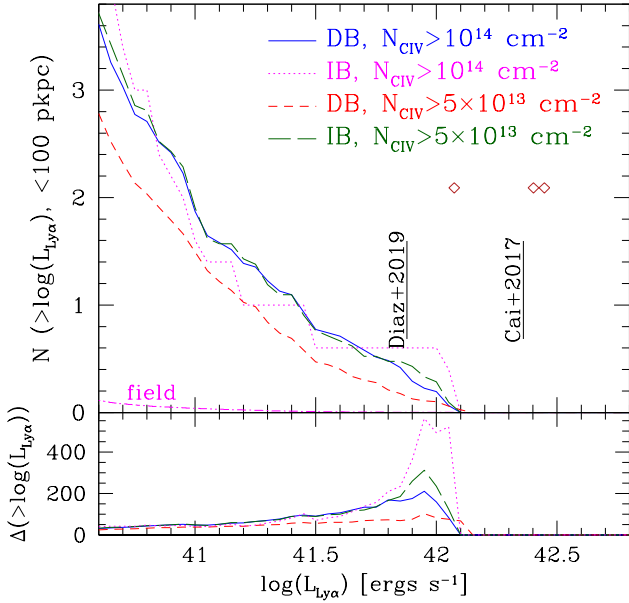


Figure 13. *Top:* The predicted average number of detectable galaxies within 100 pkpc of a CIV absorber at $z = 5.75$ as a function of Ly α luminosity. Curves corresponding to different combinations of minimum N_{CIV} and escape fraction scenario are identified in the legend. The vertical segment indicates the 4σ detection limit of Cai et al. (2017b), converted to our adopted cosmology. Diamonds indicate published observed neighboring galaxies (Díaz et al. 2014; Díaz et al. 2015; Cai et al. 2017b) as well as systems matching strong CIV absorbers at $z > 5.5$ that are identified in upcoming work (Díaz et al. 2020). *Bottom:* Local galaxy overdensity.

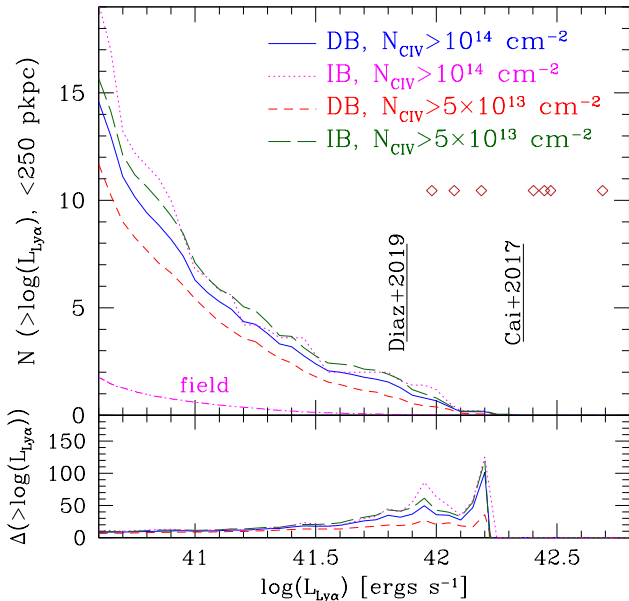


Figure 14. Same as Fig. 13 but for a maximum radius of 250 pkpc.

within 300 pkpc of strong CIV absorbers at $z > 5$, an intriguing result from Díaz et al. (2014) was the suggestion that, on scales of 10–20 comoving h^{-1} Mpc, the surface density of (bright) LBGs is systematically low in the vicinity of strong CIV absorbers while the surface density of LAEs is systematically high. Given that LAEs are fainter in the stellar continuum than LBGs, they speculated that CIV absorbers may arise preferentially in the vicinity of faint galaxies rather than bright ones. This is not expected. Figures 10–14 all indicate that the environments of strong CIV absorbers are expected to be more overdense in brighter galaxies, the opposite to what Díaz et al. (2014) infer. Subject to the (significant) caveat that our simulation does not sample bright galaxies or large spatial scales adequately to address the Díaz et al. (2014) observations directly, we may speculate qualitatively as to what the apparent disagreement suggests.

One interpretation is that the UVB’s spatial fluctuations are in reality much stronger than our model predicts. For example, we assume for simplicity that all galaxies have the same ionizing escape fraction $f_{\text{esc}}(z)$. If, instead, f_{esc} decreases with mass (Alvarez et al. 2012; Paardekooper et al. 2015; Bian et al. 2017; Steidel et al. 2018), then the dependence of overdensity on luminosity could flatten, strengthening the UVB amplitude and CIV abundance in voids. However, it is not clear that the dependence could be reversed entirely given the tendency for faint galaxies to cluster about bright ones.

An alternative explanation invokes a coincidence whereby CIV absorbers and LAEs both arise preferentially in voids, though not for the same reason. Because CIV is sensitive to He II-ionizing photons, the portion of the UVB that regulates the C III/CIV ratio remains highly inhomogeneous until He II reionization completes ($z < 3$; Miralda-Escudé 1998; McQuinn 2016). At earlier times, it is likely that He II reionization is characterized by an outside-in topology such that overdensities are more opaque at high energies than mean-density regions or voids. This topology is often seen in numerical simulations of reionization (Nakamoto et al. 2001; Finlator et al. 2009; Katz et al. 2017) and results from the tendency for ionization fronts to “leak” out of overdensities into voids. It is in fact predicted by our simulations: at $z = 5.75$, when the volume ionized fraction for He III is 50%, the ratio of the volume-averaged to the mass-averaged He III fractions is 1.5, clearly indicating that voids are more transparent to He II-ionizing photons than overdensities. If this topology is correct, then the C III/CIV ratio will inevitably be higher in overdense regions where LBGs are found. If, furthermore, C III/CIV increases more rapidly with overdensity than metallicity, then an anti-correlation between strong CIV absorbers and LBGs is expected.

In order for this phenomenology to predict an association between CIV absorbers and LAEs, it is necessary that the Ly α EW decreases with increasing overdensity. Muldrew et al. (2015) show that this could follow from quenching processes that occur predominantly in overdensities. Moreover, it is directly observed at $z \sim 3$, where clustering measurements indicate that LBGs with Ly α in emission reside preferentially in the outskirts of overdensities and in the field whereas LBGs that reside in overdensities have Lyman- α preferentially in absorption (Cooke et al. 2013). Other studies have found that narrowband-selected

LAEs are less clustered than LBGs throughout $3 < z < 7$ (Ouchi et al. 2010; Bielby et al. 2016). Likewise, studies of individual protoclusters at $3 < z < 6$ suggest that cluster members have systematically weaker Ly α emission than field galaxies of comparable luminosity (Toshikawa et al. 2016; Lemaux et al. 2018; see, however, Dey et al. (2016), who did not find this in the case of PC 217.96+32.3, which is at $z = 3.786$). Similarly, Cai et al. (2017a) note that the large-scale distribution of LAEs in the BOSS1441 field shows a broad central core that is otherwise unexpected for a proto-cluster.

A tendency for LAEs to avoid overdensities may also contribute to the result reported by Becker et al. (2018), who found an underdensity of LAEs centered about a sightline where the LAF is unusually optically thick at $z = 5.7$ (Becker et al. 2015). They attributed the LAE underdensity to the presence of a large-scale void based on modeling in which the Ly α equivalent width was assumed to have no explicit environmental dependence Davies et al. (2018). This conclusion received subsequent support from an analogous survey that uncovered a large-scale deficit of LBGs at the same redshift along the Becker et al. (2015) sightline (Kashino et al. 2019). The emerging result that, whereas regions where the LAF is unusually optically thick are associated with large-scale overdensities at $z = 2-3$ (Cai et al. 2017a), they instead trace voids at $z > 5$, may encode key insight into how galaxies drive the UVB’s evolving spatial inhomogeneity. For the present discussion, however, the Becker et al. (2015) sightline may provide only ambiguous support for the hypothesis that LAEs selectively occupy voids.

In summary, if we assume that LAEs avoid overdensities at $z \sim 6$, then they could be physically associated with strong CIV absorbers owing to a coincidence: During the outside-in stage of He II reionization, faint galaxies that cluster about LBGs are not visible as LAEs, and their CGM is not visible in CIV. By contrast, voids host more of the LAEs and enjoy higher He III and lower C III/CIV ratios owing to their spectrally harder UVB.

5 SUMMARY

We use the *Technicolor Dawn* simulations to study how systematic surveys for the neighboring galaxies of strong metal absorbers can constrain the details of the galaxy-driven reionization hypothesis. We reduce the mass flux in star formation-driven outflows by 37% with respect to Finlator et al. (2018) in order to improve agreement with observations of the galaxy stellar mass function; this reduction is within the theoretical uncertainty quoted by Muratov et al. 2015. By adopting an empirical relationship between stellar mass and Ly α equivalent width, we also recover the observed Ly α LF at $z = 5.75$, suggesting that the model predicts a realistic $M_* - M_{UV}$ relationship. Adjusting $f_{esc}(z)$ down then enables excellent agreement with observations of the history of reionization and of $T_{Ly\alpha}(z)$.

These calibrations yield satisfactory out-of-the-box agreement with the observed Si IV CDD at $z = 5.75$, but the observed CIV CDD remains underproduced. Comparisons with joint observations of Si II, Si IV, C II, and CIV indicate that the lingering CIV discrepancy in Fig. 4 cannot be elim-

inated by re-scaling the overall metal yields or stellar mass density. Nonetheless, scaling up the carbon yield by a factor of 1.75 \times simultaneously eliminates disagreements with observations of C II/Si II equivalent width ratios and of the overall C II line incidence. It also alleviates but does not eliminate the CIV deficit.

As an alternative, we replace in post-processing the traditional ionization-bounded escape scenario in which f_{esc} is energy-independent with a density-bounded scenario in which f_{esc} increases with energy. In a somewhat extreme case where $f_{esc} > 80\%$ for energies above 4 Ryd, we find significantly more CIV without overproducing Si IV although in this case the C II deficit is exacerbated.

Having established that our underlying model for galaxy growth and reionization is realistic even if CIV remains enigmatic, we turn to the spatial association between galaxies and absorbers and find:

- Galaxies with $M_{UV} < -15$ are positively-correlated with CIV absorbers out to distances of at least 300 pkpc.
- The correlation strength increases identically with CIV column density and with M_{UV} and $L_{Ly\alpha}$.
- For both stellar continuum and Ly α surveys, the mean expected number of neighbors is larger for stronger absorbers, and at fixed absorber strength it is larger under the assumption of the IB escape model because more galaxies are required to create a sufficiently hard local ionizing background.
- The mean overdensity for galaxies within a few magnitudes of L_* falls from $\approx 200-300$ within 100 pkpc of a strong absorber to $\approx 40-60$ within 250 pkpc.
- The most abundant population of neighboring galaxies is too faint to be accessible to *HST*, but integral field units can already detect more than one galaxy per absorber in Ly α . Detection will become routine with *JWST*.

We propose that, if the physical association between LAEs and strong CIV absorbers at $z > 5$ is real, then it could owe to a coincidence rather than to the tendency for LAEs to dominate the UVB. In this scenario, He II reionization is more advanced in voids than in overdensities, with the result that the CGM ionization state favors CIV in voids and lower ionization states in overdensities. The observed tendency for Ly α equivalent widths to decrease with overdensity then leads naturally to a strong but coincidental association between LAEs and strong CIV absorbers.

Our results indicate that it would be interesting to survey the galaxy environments of high-redshift Si IV absorbers for two reasons. First, their overall abundance is well-reproduced and relatively insensitive to the choice of escape fraction model (Fig. 5). Second, Si IV has a lower ionization potential than CIV. As such, it is a more direct probe than CIV of the contribution that galaxies made to the latter stages of HI reionization.

Our work leaves a number of questions unanswered, among them:

- How does f_{esc} vary with frequency? How does this dependence influence the metagalactic UVB?
- If calibrating our outflow model and $f_{esc}(z)$ to observations of the galaxy stellar mass function and the mean transmission in the LAF leads naturally to good agreement with the Si IV CDD, does the stubborn discrepancy with CIV

observations imply problems with the metal yield model, binary stellar evolution effects, the relative contribution of AGN, or f_{esc} ?

- Does the dependence of galaxy overdensity on luminosity turn over or continue to grow to the higher luminosities that our limited simulation volume does not capture?
- Do the topology of He II reionization at $z > 5$ and the dependence of $\text{EW}_{\text{Ly}\alpha}$ equivalent width on overdensity predict the association between LAEs and strong CIV absorbers that was suggested by Díaz et al. (2014)?

ACKNOWLEDGEMENTS

Some simulations contributing to this work were run on NMSU's DISCOVERY cluster; for technical advice and support we thank the NMSU ICT department. Other calculations used the Extreme Science and Engineering Discovery Environment (XSEDE), which is supported by National Science Foundation grant number ACI-1548562; we thank M. Tatineni for technical support with those efforts. We also thank V. Eijkhout for his assistance with code optimization, which was made possible through the XSEDE Extended Collaborative Support Service (ECSS) program. KF thanks G. Becker, T. Suarez Noguez, E. Ryan-Weber, C. Steidel, X.-W. Chen, M. Prescott, and C. Doughty for helpful conversations and encouragement. We thank V. D'Odorico for sharing her SiIV measurements. KF also thanks the University of Wisconsin Astronomy Department for hosting him during July 2019. We thank the anonymous referee for many helpful suggestions that improved the paper. Our work made use of the WebPlotDigitizer tool (<https://automeris.io/WebPlotDigitizer>), for which we thank A. Rohatgi, as well as E. L. Wright's online cosmology calculator (Wright 2006). This research would have been quite unthinkable without the NASA Astrophysics Data System and the arXiv eprint service. The Cosmic Dawn Center is funded by the Danish National Research Foundation.

ORCID IDS

Kristian Finlator <https://orcid.org/0000-0002-0496-1656>
C. Gonzalo Díaz <https://orcid.org/0000-0001-5146-1358>
Zheng Cai <https://orcid.org/0000-0001-8467-6478>

REFERENCES

- Alexandroff R. M., Heckman T. M., Borthakur S., Overzier R., Leitherer C., 2015, *ApJ*, **810**, 104
- Alvarez M. A., Finlator K., Trenti M., 2012, *ApJ*, **759**, L38
- Asplund M., Grevesse N., Sauval A. J., Scott P., 2009, *ARA&A*, **47**, 481
- Atek H., Richard J., Kneib J.-P., Schaerer D., 2018, *MNRAS*, **479**, 5184
- Becker G. D., Sargent W. L. W., Rauch M., Calverley A. P., 2011, *ApJ*, **735**, 93
- Becker G. D., Bolton J. S., Madau P., Pettini M., Ryan-Weber E. V., Venemans B. P., 2015, *MNRAS*, **447**, 3402
- Becker G. D., Davies F. B., Furlanetto S. R., Malkan M. A., Boera E., Douglass C., 2018, preprint, ([arXiv:1803.08932](https://arxiv.org/abs/1803.08932))
- Becker G. D., et al., 2019, arXiv e-prints, p. [arXiv:1907.02983](https://arxiv.org/abs/1907.02983)
- Behrens C., Dijkstra M., Niemeyer J. C., 2014, *A&A*, **563**, A77
- Berg D. A., Chisholm J., Erb D. K., Pogge R., Henry A., Olivier G. M., 2019, *ApJ*, **878**, L3
- Bhatawdekar R., Conselice C. J., Margalef-Bentabol B., Duncan K., 2019, *MNRAS*,
- Bian F., Fan X., McGreer I., Cai Z., Jiang L., 2017, *ApJ*, **837**, L12
- Bielby R. M., et al., 2016, *MNRAS*, **456**, 4061
- Boera E., Becker G. D., Bolton J. S., Nasir F., 2019, *ApJ*, **872**, 101
- Bosman S. E. I., Fan X., Jiang L., Reed S. L., Matsuoka Y., Becker G. D., Haehnelt M. G., 2018, preprint, ([arXiv:1802.08177](https://arxiv.org/abs/1802.08177))
- Bouwens R. J., et al., 2015, *ApJ*, **803**, 34
- Bouwens R. J., Smit R., Labbé I., Franx M., Caruana J., Oesch P., Stefanon M., Rasappu N., 2016, *ApJ*, **831**, 176
- Bromm V., Kudritzki R. P., Loeb A., 2001, *ApJ*, **552**, 464
- Cai Z., et al., 2017a, *ApJ*, **839**, 131
- Cai Z., Fan X., Dave R., Finlator K., Oppenheimer B., 2017b, *ApJ*, **849**, L18
- Chen H.-W., Prochaska J. X., Gnedin N. Y., 2007, *ApJ*, **667**, L125
- Chisholm J., Rigby J. R., Bayliss M., Berg D. A., Dahle H., Gladsters M., Sharon K., 2019, arXiv e-prints, p. [arXiv:1905.04314](https://arxiv.org/abs/1905.04314)
- Codoreanu A., Ryan-Weber E. V., García L. Á., Crighton N. H. M., Becker G., Pettini M., Madau P., Venemans B., 2018, *MNRAS*, **481**, 4940
- Conroy C., Kratter K. M., 2012, *ApJ*, **755**, 123
- Cooke J., Omori Y., Ryan-Weber E. V., 2013, *MNRAS*, **433**, 2122
- Cooper T. J., Simcoe R. A., Cooksey K. L., Bordoloi R., Miller D. R., Furezs G., Turner M. L., Bañados E., 2019, arXiv e-prints, p. [arXiv:1901.05980](https://arxiv.org/abs/1901.05980)
- D'Aloisio A., McQuinn M., Davies F. B., Furlanetto S. R., 2018, *MNRAS*, **473**, 560
- D'Odorico V., et al., 2013, *MNRAS*, **435**, 1198
- Davies F. B., Becker G. D., Furlanetto S. R., 2018, *ApJ*, **860**, 155
- Dey A., Lee K.-S., Reddy N., Cooper M., Inami H., Hong S., Gonzalez A. H., Jannuzi B. T., 2016, *ApJ*, **823**, 11
- Díaz C. G., Ryan-Weber E. V., Cooke J., Pettini M., Madau P., 2011, *MNRAS*, **418**, 820
- Díaz C. G., Koyama Y., Ryan-Weber E. V., Cooke J., Ouchi M., Shimasaku K., Nakata F., 2014, *MNRAS*, **442**, 946
- Díaz C. G., Ryan-Weber E. V., Cooke J., Koyama Y., Ouchi M., 2015, *MNRAS*, **448**, 1240
- Díaz C. G., Ryan-Weber E., Karman W., Caputi K., Salvadori S., Crighton N., Ouchi M., Vanzella E., 2020, arXiv e-prints, p. [arXiv:2001.04453](https://arxiv.org/abs/2001.04453)
- Doughty C., Finlator K., Oppenheimer B. D., Davé R., Zackrisson E., 2018, *MNRAS*, **475**, 4717
- Drake A. B., et al., 2017, *A&A*, **608**, A6
- Duncan K., Conselice C. J., 2015, *MNRAS*, **451**, 2030
- Duncan K., et al., 2014, *MNRAS*, **444**, 2960
- Eilers A.-C., Davies F. B., Hennawi J. F., 2018, *ApJ*, **864**, 53
- Eldridge J. J., Stanway E. R., Xiao L., McClelland L. A. S., Taylor G., Ng M., Greis S. M. L., Bray J. C., 2017, *Publ. Astron. Soc. Australia*, **34**, e058
- Ellis R. S., 2014, arXiv e-prints, p. [arXiv:1411.3330](https://arxiv.org/abs/1411.3330)
- Faucher-Giguère C.-A., Lidz A., Zaldarriaga M., Hernquist L., 2009, *ApJ*, **703**, 1416
- Faucher-Giguère C.-A., Hopkins P. F., Kereš D., Muratov A. L., Quataert E., Murray N., 2015, *MNRAS*, **449**, 987
- Finkelstein S. L., et al., 2015, *ApJ*, **810**, 71
- Finkelstein S. L., et al., 2019, arXiv e-prints,
- Finlator K., Özel F., Davé R., Oppenheimer B. D., 2009, *MNRAS*, **400**, 1049
- Finlator K., Oh S. P., Özel F., Davé R., 2012, *MNRAS*, **427**, 2464
- Finlator K., Oppenheimer B. D., Davé R., Zackrisson E., Thompson R., Huang S., 2016, *MNRAS*, **459**, 2299
- Finlator K., Keating L., Oppenheimer B. D., Davé R., Zackrisson E., 2018, *MNRAS*, **480**, 2628
- Fletcher T. J., Tang M., Robertson B. E., Nakajima K., Ellis R. S., Stark D. P., Inoue A., 2019, *ApJ*, **878**, 87

- Grazian A., et al., 2015, *A&A*, **575**, A96
- Haardt F., Madau P., 2012, *ApJ*, **746**, 125
- Hafen Z., et al., 2019, *MNRAS*, **488**, 1248
- Hjorth J., et al., 2003, *Nature*, **423**, 847
- Iliev I. T., Mellema G., Ahn K., Shapiro P. R., Mao Y., Pen U.-L., 2014, *MNRAS*, **439**, 725
- Inoue A. K., Iwata I., 2008, *MNRAS*, **387**, 1681
- Izotov Y. I., Schaerer D., Thuan T. X., Worseck G., Guseva N. G., Orlitová I., Verhamme A., 2016, *MNRAS*, **461**, 3683
- Izotov Y. I., Schaerer D., Worseck G., Guseva N. G., Thuan T. X., Verhamme A., Orlitová I., Fricke K. J., 2018a, *MNRAS*, **474**, 4514
- Izotov Y. I., Worseck G., Schaerer D., Guseva N. G., Thuan T. X., Fricke Verhamme A., Orlitová I., 2018b, *MNRAS*, **478**, 4851
- Jeeson-Daniel A., Ciardi B., Graziani L., 2014, *MNRAS*, **443**, 2722
- Kakiichi K., Gronke M., 2019, arXiv e-prints, p. [arXiv:1905.02480](https://arxiv.org/abs/1905.02480)
- Kakiichi K., et al., 2018, preprint, ([arXiv:1803.02981](https://arxiv.org/abs/1803.02981))
- Kashino D., Lilly S. J., Shibuya T., Ouchi M., Kashikawa N., 2019, arXiv e-prints, p. [arXiv:1909.09077](https://arxiv.org/abs/1909.09077)
- Katz H., Kimm T., Sijacki D., Haehnelt M. G., 2017, *MNRAS*, **468**, 4831
- Keating L. C., Puchwein E., Haehnelt M. G., Bird S., Bolton J. S., 2016, *MNRAS*, **461**, 606
- Khair V., Srikanth R., 2019, *MNRAS*, **484**, 4174
- Khusanova Y., et al., 2019, arXiv e-prints,
- Kimm T., Cen R., 2014, *ApJ*, **788**, 121
- Kimm T., Blaizot J., Garel T., Michel-Dansac L., Katz H., Rosdahl J., Verhamme A., Haehnelt M., 2019, *MNRAS*, **486**, 2215
- Konno A., et al., 2018, *PASJ*, **70**, S16
- Kulkarni G., Rollinde E., Hennawi J. F., Vangioni E., 2013, *ApJ*, **772**, 93
- Lemaux B. C., et al., 2018, *A&A*, **615**, A77
- Livermore R. C., Finkelstein S. L., Lotz J. M., 2017, *ApJ*, **835**, 113
- Ma X., Hopkins P. F., Kasen D., Quataert E., Faucher-Giguère C.-A., Kereš D., Murray N., Strom A., 2016, *MNRAS*, **459**, 3614
- Madau P., Ferguson H. C., Dickinson M. E., Giavalisco M., Steidel C. C., Fruchter A., 1996, *MNRAS*, **283**, 1388
- McQuinn M., 2016, *ARA&A*, **54**, 313
- McQuinn M., Oh S. P., Faucher-Giguère C.-A., 2011, *ApJ*, **743**, 82
- Meyer R. A., Bosman S. E. I., Kakiichi K., Ellis R. S., 2019, *Monthly Notices of the Royal Astronomical Society*, **483**, 19
- Miralda-Escudé J., 1998, *The Astrophysical Journal*, **501**, 15
- Muldrew S. I., Hatch N. A., Cooke E. A., 2015, *MNRAS*, **452**, 2528
- Muratov A. L., Kereš D., Faucher-Giguère C.-A., Hopkins P. F., Quataert E., Murray N., 2015, *MNRAS*, **454**, 2691
- Nakamoto T., Umehara M., Susa H., 2001, *MNRAS*, **321**, 593
- Nomoto K., Tominaga N., Umeda H., Kobayashi C., Maeda K., 2006, *Nuclear Physics A*, **777**, 424
- Oñorbe J., Hennawi J. F., Lukić Z., Walther M., 2017, *ApJ*, **847**, 63
- Oppenheimer B. D., Davé R., 2008, *MNRAS*, **387**, 577
- Ouchi M., et al., 2010, *ApJ*, **723**, 869
- Oyarzún G. A., Blanc G. A., González V., Mateo M., Bailey John I. I., 2017, *ApJ*, **843**, 133
- Paardekooper J.-P., Khochfar S., Dalla Vecchia C., 2015, *MNRAS*, **451**, 2544
- Pawlik A. H., Schaye J., van Scherpenzeel E., 2009, *MNRAS*, **394**, 1812
- Planck Collaboration et al., 2016, *A&A*, **596**, A108
- Rahmati A., Schaye J., Crain R. A., Oppenheimer B. D., Schaller M., Theuns T., 2016, *MNRAS*, **459**, 310
- Rasappu N., Smit R., Labbé I., Bouwens R. J., Stark D. P., Ellis R. S., Oesch P. A., 2016, *MNRAS*, **461**, 3886
- Rigby J., et al., 2019, *BAAS*, **51**, 245
- Rivera-Thorsen T. E., et al., 2017, *A&A*, **608**, L4
- Robertson B. E., Ellis R. S., Dunlop J. S., McLure R. J., Stark D. P., 2010, *Nature*, **468**, 49
- Robertson B. E., Ellis R. S., Furlanetto S. R., Dunlop J. S., 2015, *ApJ*, **802**, L19
- Rosdahl J., et al., 2018, preprint, ([arXiv:1801.07259](https://arxiv.org/abs/1801.07259))
- Santos S., Sobral D., Matthee J., 2016, *MNRAS*, **463**, 1678
- Schaerer D., 2002, *A&A*, **382**, 28
- Schaye J., 2006, *ApJ*, **643**, 59
- Schaye J., et al., 2010, *MNRAS*, **402**, 1536
- Shen S., Wadsley J., Stinson G., 2010, *MNRAS*, **407**, 1581
- Smit R., Bouwens R. J., Labbé I., Franx M., Wilkins S. M., Oesch P. A., 2016, *ApJ*, **833**, 254
- Somerville R. S., Davé R., 2015, *ARA&A*, **53**, 51
- Song M., et al., 2016, *ApJ*, **825**, 5
- Springel V., Hernquist L., 2003, *MNRAS*, **339**, 312
- Stanway E. R., Eldridge J. J., Becker G. D., 2016, *MNRAS*, **456**, 485
- Stark D. P., et al., 2015, *MNRAS*, **454**, 1393
- Steidel C. C., Erb D. K., Shapley A. E., Pettini M., Reddy N., Bogosavljević M., Rudie G. C., Rakic O., 2010, *ApJ*, **717**, 289
- Steidel C. C., Bogosavljević M., Shapley A. E., Reddy N. A., Rudie G. C., Pettini M., Trainor R. F., Strom A. L., 2018, *ApJ*, **869**, 123
- Tanvir N. R., et al., 2019, *MNRAS*, **483**, 5380
- Tinsley B. M., 1980, *Fundamentals of Cosmic Physics*, **5**, 287
- Toshikawa J., et al., 2016, *ApJ*, **826**, 114
- Vanzella E., et al., 2019, *MNRAS*, p. 2218
- Verhamme A., Orlitová I., Schaerer D., Hayes M., 2015, *A&A*, **578**, A7
- Wise J. H., Cen R., 2009, *ApJ*, **693**, 984
- Worseck G., et al., 2014, *MNRAS*, **445**, 1745
- Wright E. L., 2006, *PASP*, **118**, 1711
- Yan H., Windhorst R. A., 2004, *ApJ*, **600**, L1
- Yue B., et al., 2018, *ApJ*, **868**, 115
- Zackrisson E., Rydberg C.-E., Schaerer D., Östlin G., Tuli M., 2011, *ApJ*, **740**, 13
- Zackrisson E., Inoue A. K., Jensen H., 2013, *ApJ*, **777**, 39
- de La Vieuville G., et al., 2019, *A&A*, **628**, A3

APPENDIX

A Resolution Convergence

A number of numerical studies have explored the possibility that the CGM's metals can transfer between enriched and unenriched regions via small-scale diffusion processes (Shen et al. 2010; Hafen et al. 2019). For example, diffusion can strip metals from winds before they escape the ISM, decreasing the mass of metals that enters the CGM. Subsequently, it can mix metals from winds into the ambient CGM, boosting its cooling rate. Our simulation does not directly resolve processes that occur on scales smaller than $600h^{-1}$ pc (comoving). While we have not implemented a treatment for metal diffusion, we argue that doing so would not change on our predictions.

First, we limit our study to strong high-ionization absorbers. Previous work has shown that these systems trace gas whose density is between 10–1000× the cosmological mean (Rahmati et al. 2016, Fig. 8). At these densities, the impact of metal diffusion is expected to be limited, with the typical metallicity changing by 0.1–0.2 dex (Shen et al. 2010, Fig. 8). This is smaller than many of the other uncertainties mentioned in Sec. 3.4 including the choice of metal yield and escape fraction model.

Second, we have used a simple numerical convergence

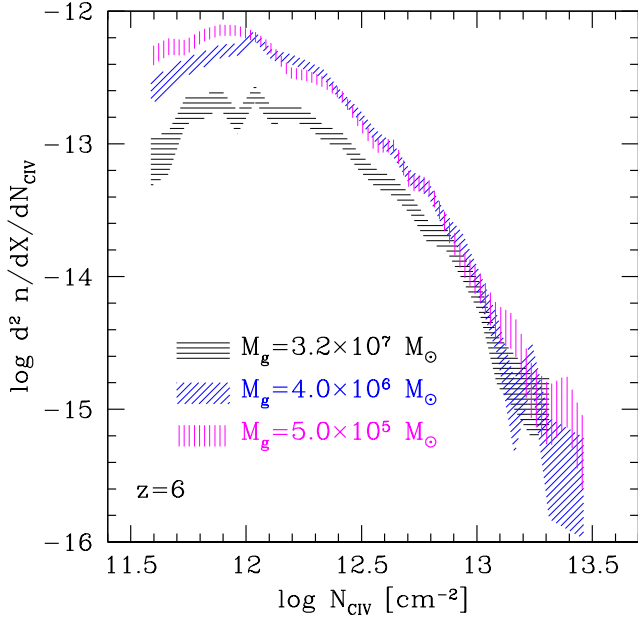


Figure A.1. Resolution convergence test for CIV CDD at $z = 6$. For $N_{\text{CIV}} > 10^{12} \text{cm}^{-2}$, convergence requires a gas particle mass of $5 \times 10^5 M_{\odot}$.

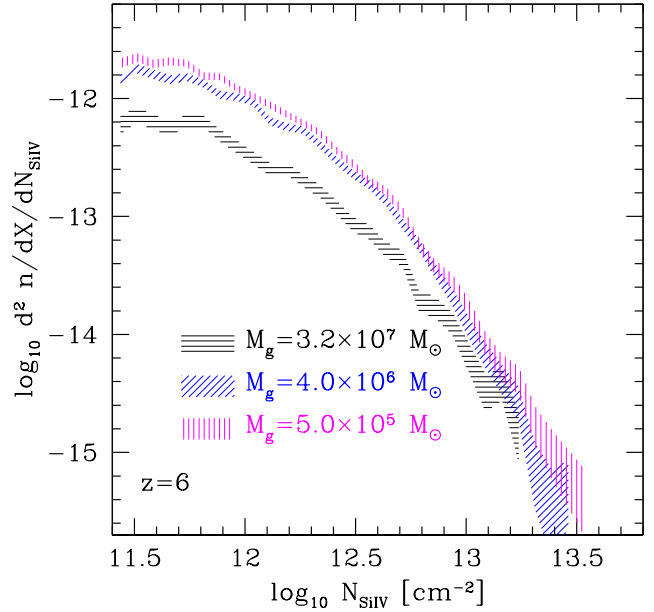


Figure A.2. Resolution convergence test for SiIV CDD at $z = 6$. For a gas particle mass of $5 \times 10^5 M_{\odot}$, the CDD is converged to 0.1 dex for all $N_{\text{SiIV}} > 10^{12} \text{cm}^{-1}$.

test to quantify overall resolution limitations. We have modeled a $15h^{-1} \text{Mpc}$ volume using three simulations that are identical except that they adopt gas particle masses M_g of 3.2×10^7 , 4.0×10^6 , and $5.0 \times 10^5 M_{\odot}$. The corresponding gas softening lengths h_{SPH} are 2.34, 1.17, and $0.59 h^{-1} \text{kpc}$ (comoving). For consistency, all simulations adopt the spatially-homogeneous Haardt & Madau (2012) UVB. Decreasing M_g generically boosts early star formation (Springel & Hernquist 2003), increasing the cosmically-averaged metallicity at early times. Decreasing h_{SPH} improves the accuracy with which small-scale mixing processes are treated. For our purposes, the most important question is whether the CIV and SiIV CDDs converge.

In Fig. A.1, we show that the CIV CDD converges for CIV column densities above 10^{12}cm^{-2} as long as $M_g < 5 \times 10^5 M_{\odot}$. At lower columns, further enhancements to the mass resolution increase the predicted line incidence. Such relatively diffuse systems are also more sensitive to sub-grid diffusion, but we do not consider them in this work. In Fig. A.2, we show that the SiIV CDD is likewise converged to within 0.1 dex at all columns if the gas resolution satisfies $M_g < 5 \times 10^5 M_{\odot}$. The simulation from which we draw this paper’s predictions has a mass resolution of $M_g = 2.6 \times 10^5 M_{\odot}$, which is higher than the three test cases considered in Figs. A.1–A.2. For both of these reasons, we believe that our predictions are insensitive to small-scale metal diffusion.

B Cosmic Variance

Our predictions may be subject to uncertainty owing to missing large-scale UVB spatial fluctuations. Fundamentally, they reflect the relationships between galaxies, their CGM, and the UVB. The physical association between

galaxies and metals is determined by inflow and feedback processes that occur on length scales of up to \sim a virial radius. For a $10^{10} M_{\odot}$ dark matter halo at $z = 6$, this is $\sim 10 \text{pkpc}$, which is several hundred times smaller than our simulation volume. Spatial correlation between galaxies and metals exists on scales of up to 300 pkpc owing to the underlying clustering of their host galaxies, but even this scale spans $< 10\%$ of our simulation volume for $z < 6$.

The ionization state of those metals, by contrast, is dominated by the UVB, which fluctuates on scales up to roughly the mean free path. At the Lyman limit, the mean free path λ_{mfp} is $10.0 \pm 1.5 \text{pMpc}$ in our cosmology at $z = 5.16$ (Worseck et al. 2014), or roughly three times as large as our simulation volume. Worseck et al. (2014) find that λ_{mfp} evolves as $(1+z)^{-5.4 \pm 0.4}$ during $2.3 < z < 5.5$. Extrapolating suggests that the simulated UVB misses large-scale fluctuations for all $z < 7$ (see also Iliev et al. 2014). The mean free path at higher energies is unconstrained. It is expected to increase with energy up to the HeII edge and then drop sharply prior to the completion of HeII reionization, with the detailed energy dependence reflecting the relative contributions of optically-thin gas versus Lyman limit systems. As reionization proceeds, large-scale UVB fluctuations must weaken the relationship between a galaxy and the ionization state of its CGM because the latter is increasingly influenced by light from distant sources rather than from the local environment. Whether this erases the predictive power of the galaxy-absorber relationship merits continued study, but even at $z = 3$ it has been argued that the local environment dominates the ionization state of self-shielded systems (Schaye 2006). We therefore expect that galaxy environments about high-ionization metal absorbers will remain sensitive to f_{esc} even within models that treat a larger dynamic range.

This paper has been typeset from a \TeX/L\AA\TeX file prepared by the author.